Nonclassical Growth Mechanism of Double-Walled Metal-Oxide Nanotubes Implying Transient Single-Walled Structures

Erwan Paineau, Franck Bourdelle, Rajesh Bhandary, Laurent Truche, Catherine Lorgeoux, Maria Bacia-Verloop, Geoffrey Monet, Stéphan Rouzière, Delphine Vantelon, Valérie Briois, et al.

Nonclassical Growth Mechanism of Double-Walled Metal-Oxide Nanotubes Implying Transient Single-Walled Structures

Erwan Paineau, Franck Bourdelle, Rajesh Bhandary, Laurent Truche, Catherine Lorgeoux, Maria Bacia-Verloop, Geoffrey Monet, Stéphan Rouzière, Delphine Vantelon, Valérie Briois, Pascale Launois

E. Paineau, R. Bhandary, G. Monet, S. Rouzière, P. Launois
Université Paris-Saclay, CNRS, Laboratoire de Physique des Solides, 91405 Orsay, France
E-mail: erwan-nicolas.paineau@universite-paris-saclay.fr; pascale.launois@universite-paris-saclay.fr

R. Bhandary
Present address: Macromolecular Chemistry, Division of Technical and Macromolecular Chemistry, Institute of Chemistry, Faculty of Natural Science II (Chemistry, Physics and Mathematics), Martin Luther University Halle-Wittenberg, von-Danckelmann-Platz 4, Halle D-06120, Germany.

G. Monet
Present address: Laboratoire de Physique de l'Ecole Normale Supérieure, ENS, Université PSL, CNRS, Sorbonne Université, Université de Paris, F-75005 Paris, France

F. Bourdelle
CY Cergy Paris Université, GEC Laboratoire Géosciences & Environnement Cergy, 95000 Neuville-sur-Oise, France

Laurent Truche
University Grenoble Alpes, CNRS, ISTerre, CS 40700, 38058 Grenoble, France

Catherine Lorgeoux
GeoRessources, UMR 7359 CNRS, Université de Lorraine, Campus Aiguillettes, 54506 Vandœuvre-lès-Nancy, France

Maria Bacia-Verloop
Institut de Biologie Structurale, CEA, CNRS, Université de Grenoble Alpes, 38027 Grenoble, France

D. Vantelon, V. Briois

Synchrotron SOLEIL, L'Orme des Merisiers, 91192 Gif-sur-Yvette Cedex, France

Keywords: Imogolite, synthesis, *in situ* monitoring, growth mechanism, multiscale approach

Abstract. The formation of imogolite nanotubes was reported to be a kinetic process involving intermediate roof-tile nanostructures. Here, we monitor in situ the structural evolution occurring during the synthesis of aluminogermanate double-walled imogolite nanotubes, thanks to an instrumented autoclave allowing the control of the temperature, the continuous measurement of pH and pressure, and the regular sampling of gas and solution. Chemical analyses confirm the completion of the precursor's conversion with the release of CO_2, ethanol and dioxane as main side products. The combination of cryo-TEM observations, infrared and XAS spectroscopies with small and wide-angle X-ray scattering experiments unravel a unique growth mechanism implying transient single-walled nanotubes instead of the self-assembly of stacked proto-imogolite tiles. The growth formation of these transient nanotubes is followed at the molecular-level by Quick-XAS experiments. Multivariate data analysis evidences that the near neighboring atomic environment of Ge evolves from monotonous to a more complex one as the reaction progresses. The following transformation into a double-walled nanotube takes place at nearly constant mean radius, as demonstrated by the simulation of X-ray scattering diagrams. Overall, transient nanotubes appear to serve for the anchoring of a new wall, corresponding to a mechanism radically different from that proposed in the literature.

1. Introduction

Hollow cylinders with a diameter in the nanometer range are carving out prime positions in nanosciences. The restricted cavity of nanotubes opens up a wide variety of applications, including selective molecular sieving, energy conversion, (photo)-catalysis and more.[1–4] Consequently, nanotubes are considered as key elements for next-generation devices in areas where ultimate nanoconfinement is crucial.[5] Beyond carbon and boron nitride nanotubes, the past years have seen the emergence of various kind of inorganic nanotubes such as chalcogenides, phosphate, polyoxometalate, rare earth, oxide/hydroxide or zeolitic nanostructures.[6–9] A recurrent concern in related researches is to elucidate the growth mechanism, a pivotal issue for the production in large quantities of defect-free nanotubes with controlled dimensions. In particular, solution growth processes often follow nonclassical pathways, involving either monomers attachment, oriented attached (OA) growth of

intermediate species, or a combination of both.[10–12] The presence of ions may also bring an additional complexity by tuning the electrostatic interactions of charged nanotubes.[13] Some challenges such as fine control of morphology are solved for inorganic imogolite nanotubes (INTs), which are aluminosilicate single-walled nanotubes with stoichiometry $SiAl_2O_7H_4$,[14] originally found in volcanic soils.[15] These nanotubes are made of a curved dioctahedral aluminum layer, the remaining octahedral space forming a vacancy on which isolated silicon tetrahedron is bonded. The nanotube strain energy presents a well-defined minimum as a function of the nanotube radius,[16,17] allowing the formation of imogolite nanotubes with monodisperse diameters at the end of the synthesis. A significant benefit of this system is the ease of producing nanotubes and their geo-inspired derivatives under mild hydrothermal conditions. Recent works proposed several pathways (varying the concentration and the nature of the precursors, pH, temperature) to obtain INTs with monodisperse diameter and chirality combined with controlled functionalization of the interfaces.[18–20] In particular, isomorphic substitution of silicon by germanium allows obtaining INTs with either single-walled (SW) or double-walled (DW) structure depending on the concentration of aluminum precursors (**Figure 1**).[21]

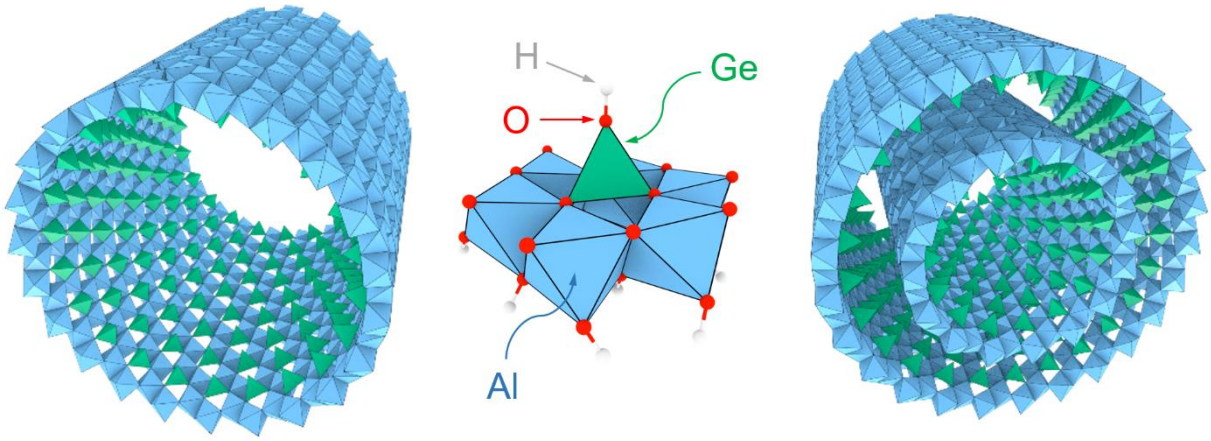

Figure 1. Atomic structure of single- and double-walled germanium-based imogolite nanotubes with a detail of the local arrangement of O_3GeOH tetrahedron (in green) with respect to the layer of $O_3Al(OH)_3$ octahedrons (in blue); O atoms are shown in red and H ones in white.

The progress in synthesis methods has brought new insights into the growth mechanism of INTs. The formation of single-walled INTs is known as a kinetic process, involving first the condensation of monomeric precursors followed by the appearance of intermediate curved structures (or proto-imogolites) that self-assembled into ring segments by an OA

mechanism.[22–26] A similar growth mechanism as for SW was tentatively advanced based on the attachment of two stacked proto-imogolites pieces to form the DW structure.[27]

The synthesis of imogolite nanotubes starts with the hydrolysis of aluminum and silicon or germanium-based precursors. It is traditionally controlled by the addition of a solution of sodium hydroxide (NaOH). A new urea based protocol was proposed in 2013.[28] The interest of this protocol lies in the formation of especially long nanotubes germanium-based Ge-DWINTs that exhibit unique liquid-crystal properties[29–31] suitable for the development of innovative functional hybrid materials.[32,33] This work focuses on elucidating the mechanisms involved during the hydrothermal synthesis of Ge-DWINTs obtained using the urea based protocol. An instrumented autoclave, originally developed for studying the long-term water-rock interactions under hydrothermal conditions,[34] has been used to follow *in situ* the change in pH of the solution formed with the initial precursors, while simultaneously collecting several liquid and gas aliquots as a function of reaction time. Gas and liquid chromatography are used to probe the completion of the reaction. The morphology and structure of the nanostructures formed in the different aliquots are investigated using cryoTEM, Small and Wide-Angle X-ray scattering (SAXS/WAXS), Infrared (IR) and X-ray Absorption Near Edge Structure (XANES) spectroscopies. Quick-X-Ray Absorption Spectroscopy (QXAS) experiments coupled with multivariate curve resolution with alternating least squares fitting (MCR-ALS) chemometrics[35,36] allow resolving at the molecular level the evolution of the speciation of Ge atoms. This experimental multi-scale approach highlights a nonclassical growth mechanism, involving the formation of transient single-walled nanotubes that further transform into Ge-DWINTs. An original signature of the transformation is the nearly constant mean radius evidenced by the simulation of WAXS results.

2. Results and Discussion

***In situ* monitoring of Ge-DWINT synthesis.** As noted above, double-walled aluminogermanate imogolite-like nanotubes were commonly synthesized below T = 100°C by hydrolyzing slowly Al and Ge precursors with a concentrated NaOH solution,[21] leading to nanotubes with a limited average length (~20 nm).[37] By contrast, longer Ge-DWINTs (> 100 nm) could be obtained in a single-step process at higher temperature (T = 140°C) using the thermal decomposition of urea $CO(NH_2)_2$ as a source of hydroxyl ions following the chemical reaction:[28,31]

$$Ge(OC_2H_5)_4 + 2Al(ClO_4)_3 + 2CO(NH_2)_2 + 9H_2O \rightarrow GeAl_2O_7H_4 + 4\,C_2H_5OH + 2CO_2{}^{\uparrow} + 2H^+ + 4\,NH_4{}^+ + 6(ClO_4)^- \quad (1)$$

Concentrations in the initial solution of tetraethoxygermanium (TEOG), aluminum perchlorate and urea are C_{Al} = 0.2 mol.L^{-1}; [Al]/[Ge] = 2, [$CO(NH_2)_2$]/[Al] = 1. Following the change in pH as a function of reaction time in strongly acidic conditions and for temperature higher than 100°C is a technical challenge. It has been achieved thanks to a dedicated autoclave lined with polytetrafluoroethylene (PTFE), equipped with pH probes and P–T sensors for *in situ* measurements during the synthesis (**Figure 2a**).[34]

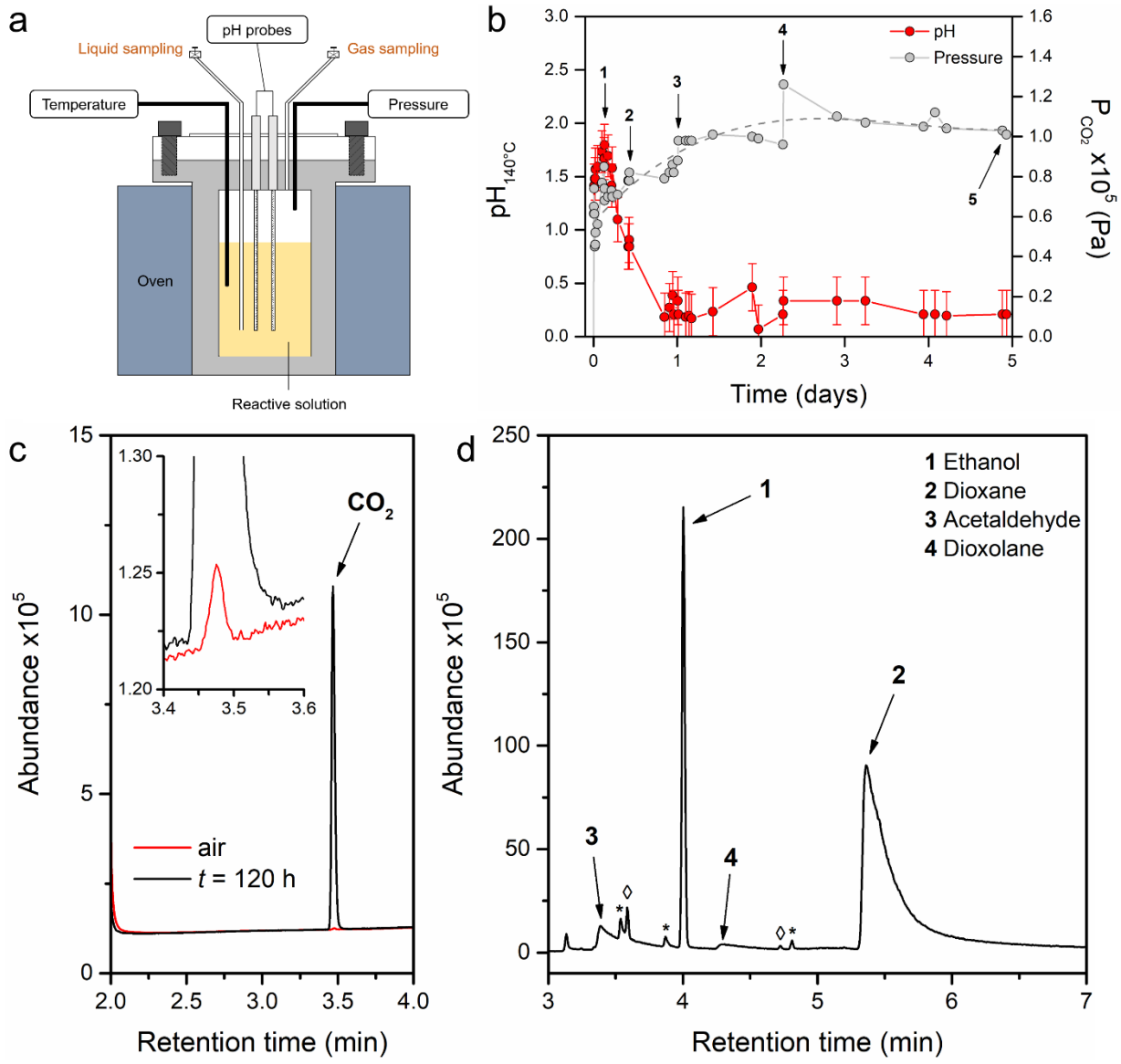

Figure 2. (a) Scheme of the experimental setup used for continuous monitoring of the hydrothermal synthesis of Ge-DWINTs. (b) Evolution of the pH of the solution and of the excess of gas pressure inside the autoclave as a function of reaction time at T = 140°C. The arrows point the moments when liquid suspension was collected. (c) GC-TCD chromatogram obtained for gas sampled at the end of the synthesis (120h), and compared to the air signal. (d) GC-MS chromatogram of the not-dialyzed end-product solution (120h, see Experimental

section). The stars indicate siloxane impurities from the septum and the column while the diamonds correspond to the signal of acetone and chloroform used for rinsing the setup. The ageing period lasts 5 days during which the pH of the solution and the pressure inside the autoclave are regularly measured (Figure 2b). In the early stages of heating (t < 3h), the pH rises from 1.2 to 1.8 along with an increase in pressure, consistent with the thermal decomposition of urea. However, the pH jump remains limited, implying that a part of the OH ions released by the decomposition of urea is consumed for the hydrolysis of the precursors.[38] Above t = 3h, the pH decreases strongly to stabilize around 0.25 after 20h, as the pressure stays nearly constant throughout the end of the heating process. A similar pH evolution has been reported previously during the growth of aluminosilicate SWINTs.[23,39] The drop in pH corresponds to the condensation of hydrolyzed precursors, which implies a release of protons according to equation 1. To go further, we then looked at identifying the resulting compounds obtained at the end of the aging stage (t = 120h). The autoclave set-up allows to sample gas and solution on-demand during the experiment thanks to two valves, one leading the gas sky and one linked to a dip tube (Figure 2a). Gas chromatography proves that only CO_2 was produced throughout the synthesis (Figure 2c), confirming the effective thermal decomposition of urea according to the reaction:

$$CO(NH_2)_2 + 3H_2O \rightarrow 2OH^- + 2\,NH_4{}^+ + CO_2{}^{\uparrow} \quad (2)$$

The excess pressure in the autoclave was therefore considered to be generated by the release of CO_2, as shown in Figure 2b (~1 bar of CO_2) and its evolution provides a qualitative vision of the urea dissociation progress. To complete this investigation, an aliquot of the recovered suspension was analyzed by gas chromatography coupled with mass spectrometry (GC-MC) (Figure 2d). As expected from eq. (1), ethanol (C_2H_5OH) is the main species obtained at the end of the reaction. We also note the presence of dioxane ($C_4H_5O_2$) and to a lesser extent acetaldehyde (CH_3CHO) and dioxolane ($C_3H_6O_2$). All these compounds originate from the recombination of alkoxide groups released during the hydrolysis and condensation of the precursors, probably through oxolation reactions.[40] Combined with the release of H^+ ions, these findings confirm for the first time the accuracy of the reaction pathway proposed in equation 1. Beyond following the evolution of pH, the main advantage of the experimental setup is to allow one to take aliquots at chosen reaction times. Several samples were collected at t = 3, 10, 24, 54 and 120h (Figure 2b). It can be pointed out that during sampling, the surrounding vapor phase is disturbed, which results in a variation of the pressure. Prior to characterizations, the collected samples were dialyzed to withdraw residual salts and organic species.

Evolution of the morphology during the reaction time. Imogolite nanotubes are very sensitive to electron beam, which limits the use of conventional TEM to get high-resolution images. By contrast, cryo-TEM experiments offer an in-depth insight of the morphology. Representative cryo-TEM images at different stages of the synthesis are presented in Figure 3 and Figures S1-S3. A first observation is the fast formation of nanotubes as early as 3h of reaction time, without the presence of proto-imogolite nanostructures (Figure 3a). The onset of the tubular morphology during the hydrothermal synthesis has been largely debated in the literature. Wilson *et al*. observed Si-SWINTs only 20h after the start of heating (T = 98°C) while only proto-imogolites were present for shorter times (< 6h).[41] However, further recent investigations showed that short Si- or Ge-SWINTs are formed in the first hours of the heating stage in coexistence with proto-imogolites.[25,42] Our findings corroborate the general trend of a rapid growth of INTs although the conditions used here imply a decomposition of urea instead of the addition of OH ions. We also notice that the nanotubes walls are not completely straight. This could be due to incomplete structuring of the nanotube wall due to the presence of some defects. More remarkable is the morphology of the nanotubes collected after 3h reaction time. Instead of DWINTs as expected with this protocol, the obtained nanotubes display a single-walled shape. Cryo-TEM observations performed on samples collected after 10 and 24 hours reaction times show new features, not observed for the 3 hours sample. Some SW nanotubes appear to co-assemble (Figure 3b). We evidence mixed SW-DW structures over the nanotube length (Figure 3b and Figure S1) as well as one-sided nanoscrolls (Figure 3c and Figures S2 and S3). These new structures seem to form by using the SW nanotubes as starting material. At the end of the synthesis (120h reaction time), all the nanotubes display a DW type morphology (Figure 3d). These observations clearly evidence an unexpected growth mechanism implying the formation of an intermediate SW structure, at the basis of the formation of the DW nanotubes.

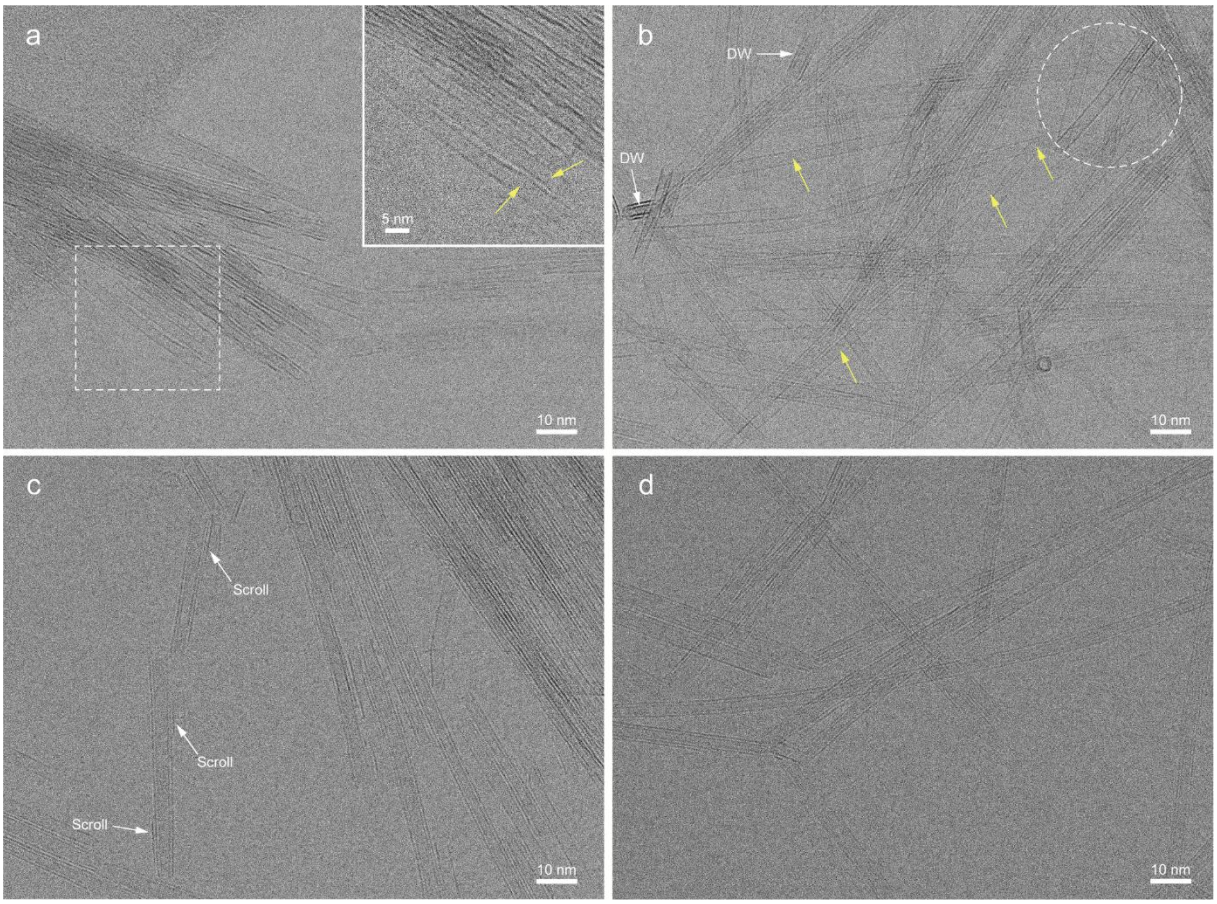

Figure 3. Representative cryo-TEM images of samples collected after (a) 3h, (b) 10h, (c) 24h and (d) 120h of reaction time. Yellow arrows point to SW nanotubes shape. The inset in panel (a) corresponds to a zoom of the area out lined in white. The circle in panel (b) illustrates a SW/DW junction.

Structural characterization of the SW to DW transformation. Small and wide-angle X-ray scattering (SAXS/WAXS) experiments have been performed to assess the nanotube shape evolution over a wide range of scattering modulus Q (see Method section). SAXS/WAXS data of Ge-INT suspensions collected at different reaction times are reported in Figure 4a. Below $Q < 0.04$ Å^{-1}, the decay of the scattered intensity follows a power-law dependence in Q^{-1} (see Figure S4 with the $Q.I(Q)$ plot of the SAXS data). This result holds for all aliquots collected at different times, from t = 3h to t = 120h. Such a power-law dependence is characteristic of 1D objects and it is thus fully compatible with cryo-TEM observations. In addition, the SAXS diagrams display several peaks corresponding to the colloidal organization of the nanotubes, which has already been studied in several articles[29,31] and are detailed in Supporting Information.

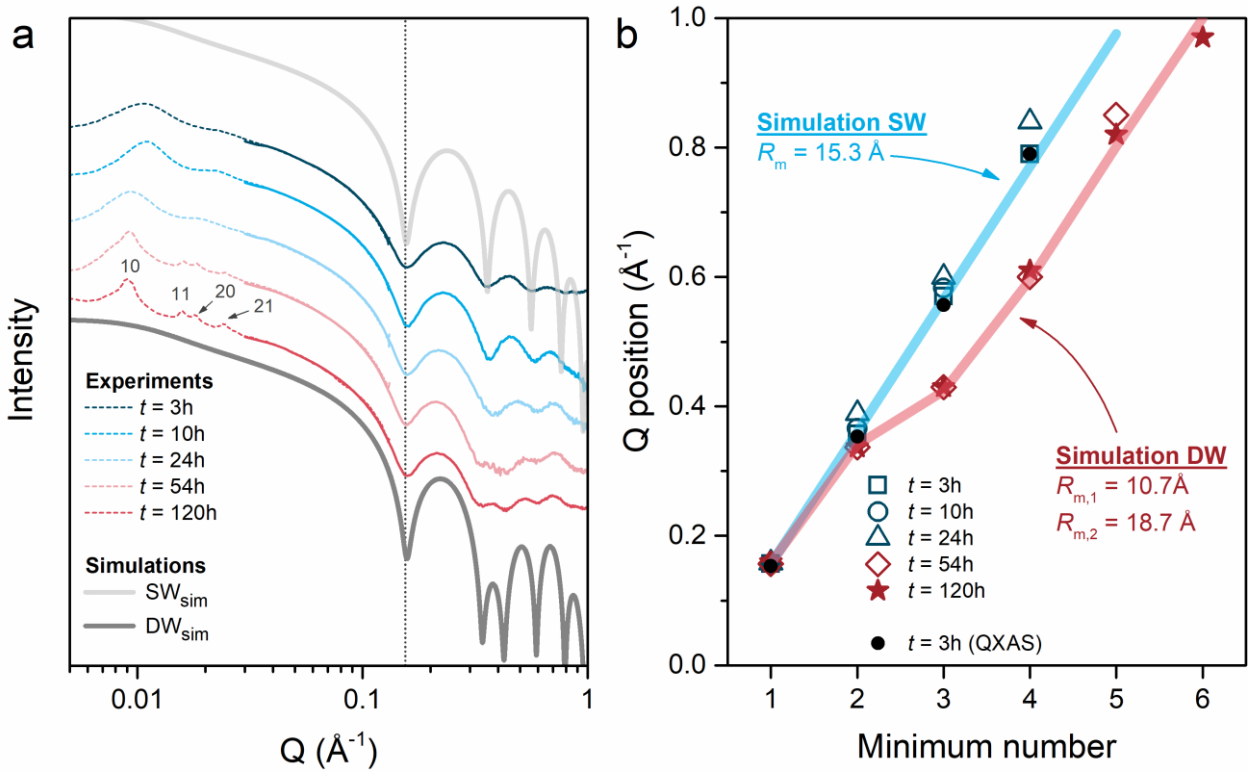

Figure 4. (a) Combined SAXS (dashed curves) and WAXS (solid curves) diagrams of Ge-INT suspensions collected at different reaction times. Light and dark grey curves correspond respectively to the calculated diagrams of SW and DW Ge-INTs of infinite length with random orientations (see text for details). Intensity is plotted in log scale. Curves are translated vertically for the sake of clarity. The Miller indices *hk* refer to the 2D hexagonal reciprocal lattice peaks. The vertical dotted line illustrates the invariance of the position of the first minimum. (b) Evolution of the position of the minima of the tubular form factor for the different samples (symbols), together with positions calculated depending on the mean values of the wall radii (see the text). Calculated positions are connected through solid lines for better visualization. In abscissa, *n* value refers to the *n*th minimum of the X-ray scattering diagram. The black dots correspond to the un-dialyzed sample recovered from QXAS experiments (see text for details).

The nanotube form factor exhibits broad oscillations between 0.1 and 1 $Å^{-1}$. They are characteristic of the radial shape of the tubes. Diagrams obtained at 3, 10 and 24h display oscillations that hamper with the increase of the scattering vector modulus, characteristic of SW nanotubes. At higher reaction time (54 and 120h), more intense modulations are observed between 0.4 and 1 $Å^{-1}$, which are caused by interferences between inner and outer walls of DW nanotubes.[43] The positions of the minima of the WAXS diagrams are plotted in Figure 4b. They are the same for 3, 10 and 24h and for 54 and 120h. To go further in the

interpretation of the WAXS data, we demonstrate in Supporting Information that these minima positions depend only on the mean nanotube radius R_m for SW nanotubes and on the mean radii $R_{m,1}$ and $R_{m,2}$ of the inner and outer walls for DW nanotubes (Figures S5 and S6). They do not depend significantly on the wall thickness e for thicknesses up to 6Å, which is the value taken for SW and DW walls.[28,44] Determined mean radii are R_m = 15.3Å for SWINTs and $R_{m,1}$ = 10.7Å, $R_{m,2}$ = 18.7Å for DW ones (equations (S5) and (S6), Figure S7). The corresponding minima positions of the WAXS diagrams are shown in Figure 4b and they fit well the minima positions obtained experimentally. Scattering diagrams are calculated from equations (S1) and (S2) for e = 6Å, corrected for geometry and polarization effects as detailed previously[44] and convoluted to the experimental resolution. They are drawn in Figure 4a, displaying good agreement with measured diagrams. X-ray scattering being a method of analysis that provides information on the major components of the system studied, the analysis of WAXS diagrams shows that the majority of these tubes are single-walled nanotubes for reaction times less than or equal to 24h and that they are double-walled tubes for reaction times greater than or equal to 54h, the radius of the single-walled nanotubes being between those of the DW walls ($R_{m,1}<R_m<R_{m,2}$). Mean radii of the SW and DW nanotubes are found to be very close: $R_m \sim (R_{m,1}+R_{m,2})/2 \sim 15$Å.

Changes in the vibrational characteristics of INTs. We investigated the evolution of the local structure during the transformation from SW to DW shape by infrared spectroscopy (Figure 5a). All spectra present a broad band between 3000 and 3800 cm^{-1} corresponding to the stretching vibration of the OH entities of imogolite nanotubes, to water molecules present inside or around the nanotubes as well as to an overtone of the OH bending mode located at 1640 cm^{-1}.[45] Two other residual IR bands are observed at 1400 and around 1100 cm^{-1}, related to NH_4^+ and ClO_4^- vibrations respectively. These species are issued from the decomposition of the precursors (see equation 1)[46,47] that are largely but not completely removed after dialysis as shown previously.[48]

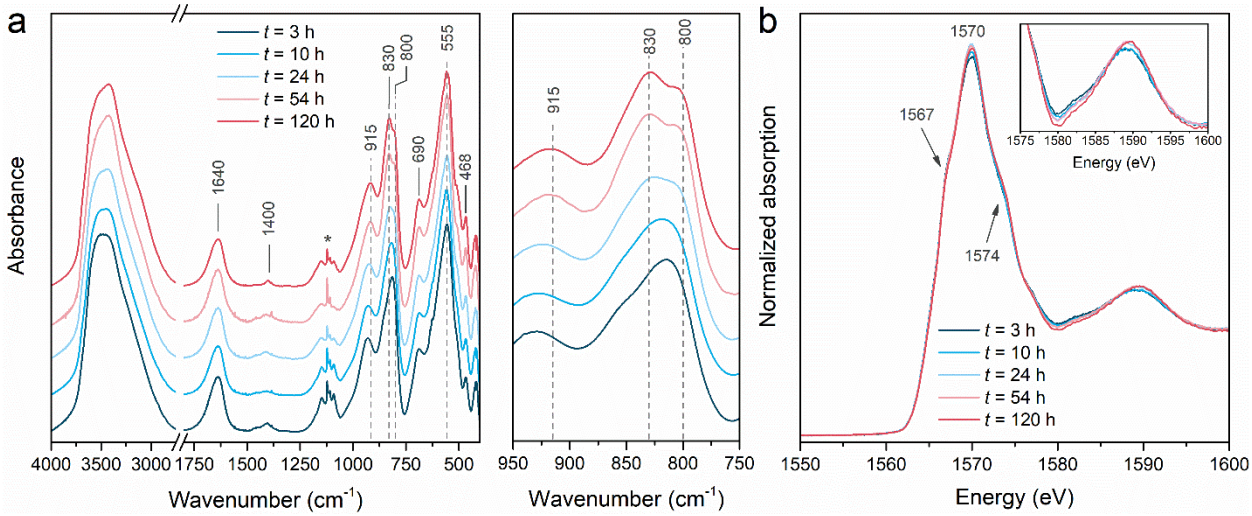

Figure 5. (a) Evolution of the IR spectra of Ge-INT samples collected at different reaction times. The right panel is a magnification of the 950-750 cm^{-1} region. Curves are translated for the sake of clarity. The star indicates the vibrational bands characteristic of perchlorate anions. (b) Corresponding XANES spectra recorded at the Al K-edge for the different samples. Inset: zoom on the 1575-1600 eV region.

The mid-infrared region below 1000 cm^{-1} corresponds to vibrations within the nanotube. Typically, the absorption bands at 690, 555 and 420 cm^{-1} refer to Al-O stretching and O-Al-O bending modes while the mode at 468 cm^{-1} is attributed to O-Ge-O bending mode.[31,49] We did not notice any significant changes for these modes throughout the synthesis. However, modifications of IR spectra during the reaction are evidenced between 950 and 750 cm^{-1} as highlighted in Figure 5a. In particular, the IR spectrum of the sample collected after 3h shows only two broad modulations at 930 and 810 cm^{-1} assigned to Ge-O stretching vibrations.[49] With increasing the reaction time, the first band is progressively red-shifted to 915 cm^{-1} while the second Ge-O stretching mode splits into two bands located at 830 and 800 cm^{-1} beyond 24h. The presence of this doublet was considered as a spectral feature related to the tubular morphology of imogolite compared to proto-imogolites that display only a broad modulation.[27] However, we do not observe with cryo-TEM the presence of proto-imogolite in samples extracted after 3 or 10h of reaction time. An alternative explanation on this band broadening could be attributed to the presence of defects into the nanotube structure as shown recently for nanotubes synthesized with different precursor ratios.[50] We also note that the evolution of the band at 855 cm^{-1}, related to deformation of OH groups linked to 2 Al atoms,[45] becomes less pronounced as the hydrothermal treatment advances. The evolution of Ge-O-Al vibrations with the reaction time suggests a growth mechanism based on a progressive structural reorganization from defective nanotubes towards nanotubes with a

stoichiometry closer to the ideal one, namely $GeAl_2O_7H_4$. To complete this investigation, X-ray Absorption Near Edge Structure (XANES) spectra were recorded at the Al K-edge (Figure 5b). The spectra display an intense sharp resonance located at 1570 eV with two shoulders at 1567 and 1574 eV. These absorption characteristics are due to the electric dipolar transitions of the Al core electrons (1s) to the first empty electronic bound states (2p) of Al in octahedral symmetry as reported previously.[51,52] Whatever the reaction time, all spectra are almost identical, corresponding to a di-octahedral Al environment. However, the broad component between 1580 and 1595 eV, related to multiple scattering effects around the nearest atomic neighbors, tends to become more intense with increasing the reaction time. This indicates a progressive increase of Al site symmetry, i.e. less dispersion in atomic distances with the progress of the reaction.

Following nanotube formation at the atomic level. The above results evidence that SW Ge-INTs form rapidly in the first hours of the reaction. In order to better understand their growth, we performed *in situ* Quick-X-ray Absorption Spectroscopy (QXAS) measurements at the Ge K-edge. These experiments were performed in a dedicated liquid cell (Figure S8), which allowed using low volume of sample (150 µL) while providing sufficient signal for measurements in transmission. The spectra were recorded every 0.25s from room temperature up to 140°C during two hours, the target temperature being reached after 10 min. In order to obtain a good signal/noise ratio, 500 successive spectra that were first interpolated in a common energy grid, have been merged leading to one spectrum every 250s. Figure 6a displays the evolution of XANES spectra collected as a function of the reaction time.

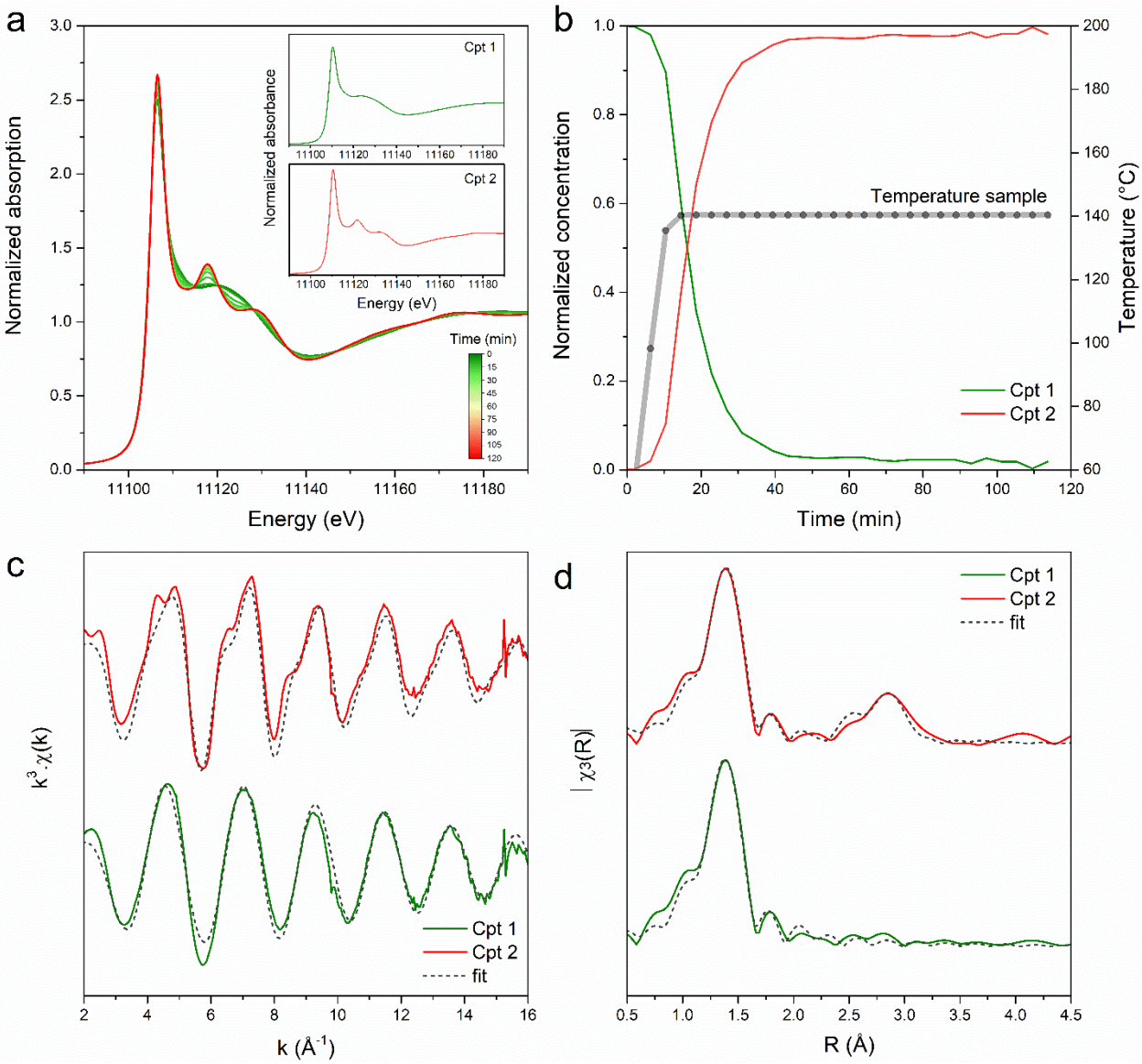

Figure 6. (a) XANES spectra evolution (dark green to red) as a function of time during the hydrothermal growth of Ge-INTs in presence of urea at 140°C. 28 averaged spectra are reported every 250s. The insets display the XANES spectra of the two pure components (Cpt) extracted by MCR-ALS analysis. (b) Profiles of concentrations of the two components as a function of the reaction time. (c) EXAFS function weighted by k^3 of the two pure components and (d) their corresponding Fourier transforms magnitudes. The curves are translated for the sake of clarity. The dotted lines corresponds to the simulations presented in Table 1.

The white line at 11106 eV does not change in position, showing the preservation of the tetrahedral geometry around Ge atoms during the hydrothermal growth. However, the broad modulation at 11122 eV decreases and splits into two distinct peaks ay 11117 and 11130 eV. This evolution clearly evidences a change in the second Ge coordination sphere, the near neighboring atomic environment evolving from monotonous to a more complex environment

as the reaction progresses. To determine the involved Ge species, the time-resolved normalized XAS dataset was analyzed by multivariate curve resolution with alternating least squares (MCR-ALS) chemometrics, a fitting procedure suitable for spectroscopic data governed by the Beer-Lambert law.[53–55] It consists in the bilinear decomposition of a matrix D_{ij} representing the *i* QXAS spectra of the sample for the *j* energy values, according to:

$$D_{ij} = CS^T + E \quad (3)$$

C and S^T are the matrices of the concentration profiles and individual XAS spectra of the pure components that best fit the experimental data, respectively. The matrix *E* contains the residual noise. In our case, the ALS minimization used for solving iteratively equation 3 started considering an initial estimate of the S^T matrix provided by using the SIMPLISMA (SIMPLe to use Interactive Self-Modelling Algorithm) method, which isolates the most dissimilar spectra from the experimental data set.[56,57] Results of MCR-ALS analysis evidence the presence of only two pure components (Cpt) throughout the reaction time (insets in Figure 6a). The initial Ge species (Cpt 1) decrease rapidly to the benefit of Cpt 2, as shown from the profiles of concentrations (Figure 6b). To confirm this result, we performed the same MCR-ALS analysis but using an average of 10 successive spectra instead of 500 (Figure S9). It does not modify the number of species involved. Most of the initial Ge configuration is converted after 40 min without involving an intermediate phase in these synthesis conditions. WAXS analysis of the sample obtained at the end of the experiment shows that it is formed of Ge-SWINTs (Figure S10). The position of the minima of the tubular form factor are with the same as those determined for nanotubes obtained for reaction times less than or equal to 24h with the instrumented autoclave (Figure 4).

The $k^3\chi(k)$ functions and the corresponding Fourier transforms magnitudes of the two components are drawn in Figure 6c and d, respectively. $\chi(k)$ is the EXAFS function ($\chi(k) = \frac{\mu(k)-\mu_0(k_0)}{\mu_0(k_0)}$ where μ and μ_0 are respectively the measured absorption coefficient and the one corresponding to isolated Ge atoms, $k = \sqrt{\frac{2m}{\hbar^2}(E - E_0)}$ with *m* the mass of the electron and E_0 the adsorption edge. The shape of Cpt 1 $k^3\chi(k)$ function shows oscillations with a single frequency, indicating the presence of a single shell of neighboring atoms in accordance with the monotonous shape of the XANES curve. Similar curves were reported for aqueous solution of germanic acid $Ge(OH)_4$.[58] This is confirmed by fitting the curve with the refined backscattering paths calculated for an isolated $Ge(OH)_4$ tetrahedron (Figure 6c,d). The fitting parameters are reported in Table 1. A good agreement is obtained by using only a single Ge-O_1-Ge path, considering that the EXAFS spectrum is related to monomers with a tetrahedral

coordination of Ge atoms. This hypothesis is reasonable since the intensity of the Fourier transform of the EXAFS spectrum of Cpt 1 is highly dampened beyond 2 Å as for the reference TEOG precursor dispersed in water (Figure S12a-c).

Table 1. Fitting parameters of the MCR-ALS calculated Ge K-edge EXAFS spectra. The Ge coordination number *N* has been set before the adjustment.

Component	Backscattering path	Coordination number N	Radial distance (Å)[a]	Debye-Waller factor (Å)
Cpt 1	Ge-O_1-Ge	4	1.75	2.3 10^{-3}
Cpt 2	Ge-O_1-Ge	4	1.76	2.6 10^{-3}
	Ge-O_2-Ge	3	3.11	6.7 10^{-3}
	Ge-Al-Ge	6	3.22	6.7 10^{-3}

[a]The uncertainty on radial distance values is ±0.01 Å.

By contrast, the Cpt 2 function is no longer monotonic, revealing the presence of additional shells of atomic neighbors. It should correspond to the local structure of Ge atoms in imogolite nanotube.[22,52,59] In this case, the curves have been fitted with refined backscattering paths calculated for the imogolite atomic structure determined in Monet et al[60] (Figure 6c,d). A schematic representation of the first three coordination spheres around the scattering atom (Ge) is also shown in Figure S11. The intensity of the Fourier transform magnitude for Cpt 2 remains high for large *R* distances, due to the presence of additional neighboring atoms at larger distance. The Ge coordination is reproduced with four O atoms in the first coordination sphere and a contribution of Al and O atoms in a second and third coordination sphere. The resulting Ge-O and Ge-Al distances corresponds well to the distances expected for an aluminogermanate imogolite nanotube, in agreement with previous works.[22,27,52]

Comparison of the EXAFS functions of Cpt 2, which is a SW nanotube, with those measured for a suspension of Ge-DWINTs are very similar (Figure S12d-f). In fact, it is not possible to distinguish between a SW and a DW tube as both nanotubes share the same local structure.[52]

Growth mechanism of Ge-DWINTs. Different models have been proposed to explain the formation and growth of imogolite nanotubes. As mentioned previously, the consensus is

reached for a kinetic process starting from the condensation of Al and Si (or Ge) precursors in intermediate proto-imogolites followed by a self-organization growth during the hydrothermal treatment.[24–26] The mechanism of SW/DW shape control proposed in the literature is based on a competition between curvature and adhesion between the inner and outer faces of the nanotubes, with the attraction of two proto-imogolite single sheets, forming a proto-imogolite double-sheet for DWINTs.[27,47] Nevertheless, the growth of Ge-DWINTs through the self-assembly of DW proto-imogolite tiles has not been demonstrated experimentally. Our *in situ* investigations prove a different mechanism for Ge-DWINTs formation, which is schematically summarized in Figure 7.

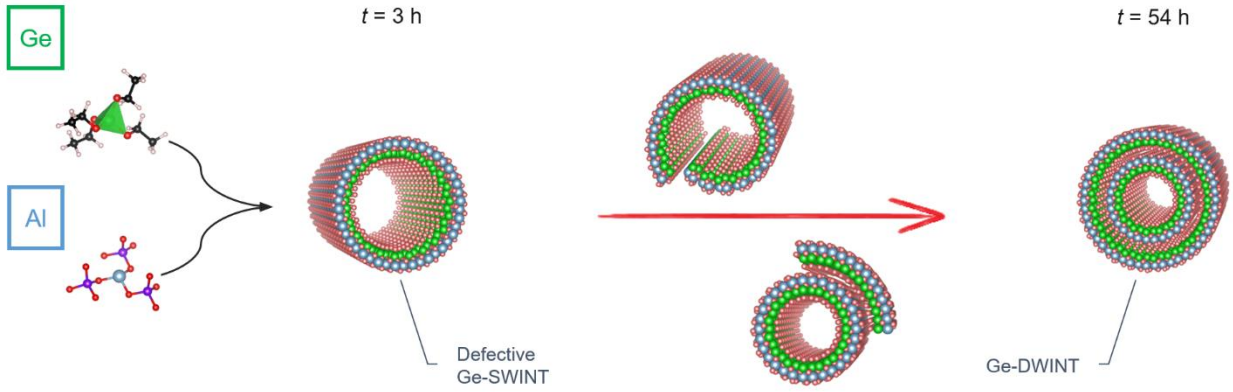

Figure 7. Schematic representation of the conversion of SW to DW during the hydrothermal synthesis using TEOG and aluminum perchlorate in presence of urea as hydrolyzing agent. The initial SW INTs are progressively transformed into DW INTs, involving transient nanoscrolls and/or mixed SW-DW structures.

First, we evidence the formation of Ge-SWINTs instead of DW nanostructures during the hydrothermal synthesis. These Ge-SWINTs appears very quickly (t < 3h) through the hydroxylation and condensation of Al and Ge monomers. In particular, the MCR-ALS analysis of QXAS dataset allows us to assert that the growth is achieved by the direct conversion of Ge monomers without any intermediate species. The early formed structures recovered after few hours of hydrothermal treatment display a SW signature and are probably defective. Indeed, IR measurements show poorly defined Ge-O stretching modes around 810 cm^{-1} for samples obtained at $t \leq$ 24h (Figure 3a). With increasing the reaction time, the vibrational characteristics of the early-formed nanotubes evolve progressively until reaching the expected infrared signal for Ge-DWINTs. The SW structures are therefore transient since they disappear over time to the benefit of double-walled nanotubes. The decrease in pH (Figure 2b) mainly occurs during the first hours of the hydrothermal treatment related to the

conversion of the precursors and the formation of transient Ge-SWINTs, implying a release of protons (Equation 1). Beyond 24h of reaction time, the pH value remains almost constant around 0.5 during the transformation of SW nanotubes into DW ones. Even if H^+ ions are released during this transformation, the pH is already very acidic limiting the evidence of a decrease in pH values.

Key to understanding the formation of DWINTs from SW ones is that the transformation occurs at nearly constant mean radius. Even if its understanding at the atomic scale remains an unsettled issue, some scenarios can already be discussed. A first model could be a growth induced by a bifurcation point (wall defect). The propagation of a DW structure on the inner wall of the Ge-SWINT should require precursors to diffuse into the nanotube to reach the SW/DW bifurcation and this growth mode could rapidly become a diffusion limited process. Therefore, a number of partially formed SW/DW nanotubes with different junction positions should be observed throughout long reaction time, which has not been identified in this work. We could also invoke a 1D Ostwald ripening growth in which transient Ge-SWINTs would be slowly re-dissolved overtime to form thermodynamically stable Ge-DWINTs but this will not explain the observed presence of nanoscrolls at intermediate times. Alternatively, we propose that the Ge-DWINTs are formed by overgrowth of the second wall from the first one leading to complex nanotubes with locally an additional wall as highlighted by cryo-TEM observations (t = 10h and 24h). The original growth mechanism of DW INTs evidenced here raises the question of revisiting the growth of DW INTs in different conditions (effect of the temperature, change of the OH source…). To the best of our knowledge, only Maillet et al. investigated the growth of DW nanotubes by in-situ SAXS experiments but the maximum *Q*-value was below 0.5 $Å^{-1}$, limiting morphology differentiation on the basis of form factor.[24] Moreover, our methodology could bring new insights on the formation of other inorganic nanotubes such as $Co(OH)_2$, which display various intermediate morphologies (SW, DW, spirals, interlaced nanotubes) in similar synthesis conditions.[7]

3. Conclusion

In summary, the use of a hydrothermal reactor vessel coupled with pH and pressure probes allow to monitor for the first time the growth of double-walled imogolite nanotubes under hydrothermal conditions. Chemical analyses confirm the completion of the precursor's conversion with CO_2, ethanol and dioxane as main by-products. The sampling during the synthesis enables us to trap and characterize unexpected intermediate phases. In particular, we evidence the fast formation of single-walled hollow nanotubes after few hours of thermal

treatment. *In situ* time-resolved QXAS experiments allow to determine quantitatively the evolution in the Ge environment throughout the hydrothermal synthesis. Multivariate data analysis highlights a progressive transformation of Ge monomers into Ge-SWINTs. These nanotubes appear as a transient state as they evolve in favor of double-walled aluminogermanate nanotubes. Cryo-TEM observations reveal mixed SW-DW structures over the nanotube length as well as one-sided nanoscrolls, which seem to form by using the SW nanotubes as starting material. The SW to DW transformation takes place after the first 24h of the reaction, as shown by SAXS/WAXS results. IR experiments indicate that the transient SWINTs are more defective than the final DW nanotubes. Moreover, the SW to DW transformation occurs at nearly constant average radius, as shown from WAXS analysis, which is probably a key point for further modelization of the transformation at the atomic scale. In particular, the formation of the nanoscrolls and their role in the overall process deserves further study. The growth mechanism of Ge-DWINTs mediated by transient SW nanotubes is unique in the wide family of inorganic nanotubes. Moreover, the present results offer a simple way to modify and control the morphology of these metal-oxide nanostructures by tuning the reaction time. Such nanostructures can be used for the development of specific nanocomposites.[32,61]

4. Experimental Section

Chemical products. Tetraethoxygermanium (TEOG, ≥99.95%), aluminum perchlorate (ACS reagent, ≥98%) and urea ($CO(NH_2)_2$, ACS reagent, 99%) were purchased from Sigma Aldrich. All products were used as received. Synthesis and dialyses were performed using Milli-Q water.

Description of the instrumented reactor. Immediately after mixing the precursors, the solution was transferred in a 316L stainless-steel autoclave (MAXIMATOR®, France) fitted with a PTFE liner and heated by an external collar furnace at 140°C. Pressure and temperature probes are connected to a nanodac™ monitor, recording continuously P-T data with an accuracy of 0.1 bar and 0.1°C, respectively. The target temperature was reached in less than 30 min. In situ pH measurements were performed thanks to commercial supporting-high temperature probes supplied by Corr Instruments (USA). The monitoring system consisted of a zirconia (ZrO_2-based) pH electrode (Ag/Ag_2O) coupled to an Ag/AgCl external pressure balanced reference electrode. These electrodes, tubing and connectors, have wetted metallic parts made of pure titanium grade 3. The probes were inserted through the closure of the autoclave, and connected to a high impedance pH-meter (Mettler Toledo, SevenMulti). The

electrode pair is equilibrated in heated buffers at 140 °C, and calibrated with a three-point procedure for pH (standards $pH_{25°C}$ = 4 [C_6H_4(COOH) COOK], 7 [Na_2HPO_4/KH_2PO_4] and 9 [$Na_2B_4O_7$]), before and after the run, to check the measurement deviation. The measured electromotive force exhibits high stability over long periods of time, with a drift of less than 0.05 pH units between the start and the end of the run. Calibration curves show a sub-Nernstian slope close to the theoretical value at 140°C (i.e., 78.7 mV/pH). Details on electrodes principle and calibration are given elsewhere.[62,63] Gas sampling was carried out using a sealed and flushed storage cell made of stainless steel. Liquid sampling was conducted at different times *t* = 3, 10, 24, 54 and 120h. Before further characterizations, the recovered suspensions were dialyzed 10 times against ultrapure water using semi-permeable membranes (cutoff: 10 kDan Spectra/Por®, Spectrum) until the conductivity of the washing bath was below 0.5 $mS.m^{-1}$. In addition, an aliquot for *t* = 120h was not dialyzed in order to identify the species resulting from the synthesis reaction.

Gas and solution analysis. The gas samples were analyzed by gas chromatography (GC) coupled to a thermal conductivity detector (TCD). The chromatograph column is a Carbobond (Agilent, 50 m in length, internal diameter of 0.53 mm, film thickness of 10 μm), traversed by helium as carrier gas (constant pressure of 1.03 bar). The oven temperature program was: (i) 30°C during 2 min, (ii) a heating ramp at 50°C/min, (iii) 180°C during 5 min.[64] To obtain precise identification of Ar, CO_2 and H_2 gases, the TCD was previously calibrated using several Ar + H_2 + CO_2 mixtures of different concentrations at various pressures injected from an injection loop of 20 μl. In these conditions, the detection limit is 3 mbar for CO_2 and 8 mbar for H_2.

The extract (*t* = 120 h, no dialysis) was injected in a chromatograph coupled with a mass spectrometer (GC–MS). The gas chromatograph was an Agilent 6890N, equipped with a capillary column DB5-MS (60 m×0.25 mm i.d. ×0.25 μm film thickness). The oven temperature program was as follow: at 70 °C for 2 min, from 70 °C to 130 °C at 15 °C/min, then from 130 °C to 315 °C at 4 °C/min and then a 30 min hold at 315 °C. The carrier gas was helium at 1.6 mL/min constant flow. The injector temperature was set at 300 °C and injections were done with 1 μL of extracts in splitless mode. The GC was coupled to an Agilent 5973 mass spectrometer operating in fullscan mode. The molecules were ionized by electronic impact and the mass fragments were discriminated by a quadrupole mass analyzer. The identification of the compounds was possible using NIST and Wiley libraries.

Transmission Electron Microscopy (TEM). Cryo-TEM observations were undertaken to assess the structure of the nanotubes at the different times used for liquid sampling.

Experiments were carried out on a FEI Tecnai G2 Polara device operating at 300 kV, under low electron illumination conditions (dose < 15 $e^{-}.Å^{-2}$). The images were collected on a K2 summit direct detector (Gatan). For each sample, a drop (4 µL) of a dilute suspension (~10 $mg.L^{-1}$) was deposited on a R2/2 Quantifoil grid made hydrophilic after glow discharging. A fully automated Vitrobot (FEI) device was used to blot the grid and rapidly plunge and freeze aqueous films of the nanotubes suspension into liquid ethane cooled by liquid nitrogen, to prevent the formation of ice crystals.

Infrared spectroscopy. Aliquots of the dialyzed suspensions were dried at 60°C during 24h, the resulting sediment being milled in an agate mortar to obtain a fine powder. KBr pressed pellets were prepared by mixing ~ 1.5 mg of sample powder with 150 mg of potassium bromide. Fourier Transform Infrared (FTIR) measurements were performed with a Nicolet iS50 FTIR spectrometer equipped with a KBr beamsplitter and a DTGS/KBr detector. IR spectrum was recorded at 4 cm^{-1} resolution in transmission mode in the 4000-400 cm^{-1} range.

X-ray scattering. Dialized aqueous suspensions were held in 1 mm diameter borosilicate tubes (WJMGlas/Müller GmbH, Germany) that were flame-sealed to prevent water evaporation, and stored vertically prior to X-ray scattering measurements. Small-Angle X-ray Scattering (SAXS) experiments were realized on the D2AM beamline at European Synchrotron Radiation Facility (Grenoble, France). Measurements were conducted at a wavelength of 0.138 nm. Two-dimensional (2D) SAXS patterns were recorded using an ImXPAD (d5-S540) detector placed at a distance of 2 m of the sample. Wide-Angle X-ray Scattering (WAXS) measurements were performed on a rotating anode generator (model RUH3R, Rigaku Corp., Japan) of the MORPHEUS platform (Laboratoire de Physique des Solides) at the Mo wavelength ($\lambda_{MoK\alpha}$ = 0.0711 nm).[65] 2D-WAXS diagrams were collected on a MAR345 detector (marXperts GmBH, Germany) with 150 µm pixel size placed behind a vacuum tunnel at a distance of 728.5mm of the sample. The experimental resolution is a Gaussian function with full-width at half-maximum equal to 0.013$Å^{-1}$. Extraction of the scattered intensity I as a function of the scattering modulus Q ($Q = 4\pi/\lambda \sin\theta$, with 2θ the scattering angle) was performed with home-developed software. Background due to scattering from the capillary and water was subtracted.

X-ray absorption spectroscopy. X-ray absorption spectra at the Al K-edge were collected at the LUCIA beamline of synchrotron SOLEIL.[66] A KTP (011) double crystal was used to monochromatize the X-ray beam, whose energy was calibrated using the first inflexion point of the Al K-edge of an aluminum foil (1559 eV). Powder samples were processed as pressed pellets and placed in a primary vacuum chamber. Fly-scan XANES spectra were collected in

fluorescence mode with an energy step of 0.2 eV and a counting time of 400 ms using a 60 mm^2 mono-element silicon drift detector (Bruker). XANES data were normalized by fitting the pre-edge region with a linear function and the post-edge region with a quadratic polynomial function using the Athena software package.[67]

Quick-EXAFS at the Ge K-edge were performed on the ROCK beamline at SOLEIL using a Si (111) channel-cut monochromator installed on a tilt-table oscillating with a 2 Hz frequency, which allows for recording an EXAFS spectrum in 500 ms.[68] The energy calibration was performed by setting the first inflection point of the XANES spectrum of Ge metallic foil at 11104 eV. Measurements were carried out in transmission mode using ionization chambers (Ohyo Koken) filled with N_2. Data normalization was performed using homemade interfaces developed by the beamline team for the fast handling of the Quick-EXAFS data.[69] Data were extracted by averaging successive spectra that were first interpolated in a common energy grid in order to obtain a good signal/noise ratio. The chemometric analysis by MCR-ALS fitting was performed using the MCR-ALS GUI 2.0 free toolbox developed by Jaumot et al.[36] The rank of the experimental data matrix composed of the spectra recorded during the heating ramp was determined first by Principal Component Analysis (PCA). Two principal components were necessary for explaining the variance data set. EXAFS oscillations of the MCR-ALS isolated components were extracted using the Athena software package. The amplitude reduction factor and the energy shift were determined on the analysis of standard references and left fixed for the analysis of the MCR-ALS components. EXAFS oscillations were then fitted by using theoretical backscattering paths calculated from a reference imogolite nanotube structure[60] using the IFEFFIT code.

Supporting Information

Supporting Information is available from the Wiley Online Library or from the author.

Acknowledgements

The authors acknowledge the financial support of the French ANR agency (ANR) under grand agreement ANR-18-CE09-0001 (C3PO). RB and PL acknowledge the public grant overseen by the Region Ile-de-France in the framework of DIM Respore for RB's post-doc position. This work made use the platforms of the Grenoble Instruct-ERIC Center (ISBG: UMS 3518 CNRS-CEA-UGA-EMBL) with support from FRISBI (ANR-10 INSB-05-02) and GRAL (ANR-10-LABX-49-01) within the Grenoble Partnership for Structural Biology (PSB). Synthesis was performed using the hydrothermal experimentation platform of GeoRessources

(UMR 7359 CNRS, University of Lorraine). The authors acknowledge Synchrotron SOLEIL and the European Synchrotron Radiation Facility under the approved proposal 20200604 and 02-01-880. The construction of the ROCK beamline used for the Quick-EXAFS measurements were supported by a public grant overseen by the French National Research Agency (ANR) as part of the "Investissements d'Avenir" program (reference: ANR-10-EQPX-45). They thank Isabelle Morfin for their assistance during SAXS experiments, Laurent Barthe, Marc Bottineau and Stéphane Cabaret for the design and implementation of the cell for Quick-EXAFS experiments. The authors are particularly grateful to Gilberto Teobaldi for meaningful discussions.

Received: ((will be filled in by the editorial staff))
Revised: ((will be filled in by the editorial staff))
Published online: ((will be filled in by the editorial staff))

References

[1] H. G. Park, Y. Jung, *Chem. Soc. Rev.* **2014**, *43*, 565.
[2] B. Weng, S. Liu, Z.-R. Tang, Y.-J. Xu, *Rsc Adv.* **2014**, *4*, 12685.
[3] R. H. Tunuguntla, R. Y. Henley, Y.-C. Yao, T. A. Pham, M. Wanunu, A. Noy, *Science* **2017**, *357*, 792.
[4] A. Marcotte, T. Mouterde, A. Niguès, A. Siria, L. Bocquet, *Nat. Mater.* **2020**, *19*, 1057.
[5] L. Bocquet, *Nat. Mater.* **2020**, *19*, 254.
[6] W. Shi, S. Song, H. Zhang, *Chem. Soc. Rev.* **2013**, *42*, 5714.
[7] B. Ni, H. Liu, P. Wang, J. He, X. Wang, *Nat. Commun.* **2015**, *6*, 8756.
[8] M. Serra, R. Arenal, R. Tenne, *Nanoscale* **2019**, *11*, 8073.
[9] A. Korde, B. Min, E. Kapaca, O. Knio, I. Nezam, Z. Wang, J. Leisen, X. Yin, X. Zhang, D. S. Sholl, *Science* **2022**, *375*, 62.
[10] J. J. De Yoreo, P. U. Gilbert, N. A. Sommerdijk, R. L. Penn, S. Whitelam, D. Joester, H. Zhang, J. D. Rimer, A. Navrotsky, J. F. Banfield, *Science* **2015**, *349*, aaa6760.
[11] J. Lee, J. Yang, S. G. Kwon, T. Hyeon, *Nat. Rev. Mater.* **2016**, *1*, 1.
[12] B. Ni, X. Wang, *Chem. Sci.* **2016**, *7*, 3978.
[13] H. Liu, H. Li, X. Wang, *Small* **2016**, *12*, 2969.
[14] P. D. G. Cradwick, K. Wada, J. Russell, N. Yoshinaga, C. Masson, V. Farmer, *Nat.-Phys. Sci.* **1972**, *240*, 187.
[15] R. Dahlgren, S. Shoji, M. Nanzyo, in *Dev. Soil Sci.*, Elsevier, **1993**, pp. 101–143.
[16] L. Guimaraes, A. N. Enyashin, J. Frenzel, T. Heine, H. A. Duarte, G. Seifert, *Acs Nano* **2007**, *1*, 362.
[17] S. Konduri, S. Mukherjee, S. Nair, *Acs Nano* **2007**, *1*, 393.
[18] E. Paineau, *Appl. Sci.* **2018**, *8*, 1921.
[19] G. Monet, M. S. Amara, S. Rouzière, E. Paineau, Z. Chai, J. D. Elliott, E. Poli, L.-M. Liu, G. Teobaldi, P. Launois, *Nat. Commun.* **2018**, *9*, 2033.
[20] J. Govan, N. Arancibia-Miranda, M. Escudey, B. Bonelli, F. Tasca, *Mater. Chem. Front.* **2021**, *5*, 6779.

[21] P. Maillet, C. Levard, E. Larquet, C. Mariet, O. Spalla, N. Menguy, A. Masion, E. Doelsch, J. Rose, A. Thill, *J. Am. Chem. Soc.* **2010**, *132*, 1208.
[22] C. Levard, J. Rose, A. Thill, A. Masion, E. Doelsch, P. Maillet, O. Spalla, L. Olivi, A. Cognigni, F. Ziarelli, J.-Y. Bottero, *Chem. Mater.* **2010**, *22*, 2466.
[23] G. I. Yucelen, R. P. Choudhury, A. Vyalikh, U. Scheler, H. W. Beckham, S. Nair, *J. Am. Chem. Soc.* **2011**, *133*, 5397.
[24] P. Maillet, C. Levard, O. Spalla, A. Masion, J. Rose, A. Thill, *Phys. Chem. Chem. Phys.* **2011**, *13*, 2682.
[25] G. I. Yucelen, D.-Y. Kang, I. Schmidt-Krey, H. W. Beckham, S. Nair, *Chem. Eng. Sci.* **2013**, *90*, 200.
[26] P. Du, P. Yuan, A. Thill, F. Annabi-Bergaya, D. Liu, S. Wang, *Appl. Clay Sci.* **2017**, *150*, 115.
[27] A. Thill, P. Maillet, B. Guiose, O. Spalla, L. Belloni, P. Chaurand, M. Auffan, L. Olivi, J. Rose, *J. Am. Chem. Soc.* **2012**, *134*, 3780.
[28] M.-S. Amara, E. Paineau, M. Bacia-Verloop, M.-E. M. Krapf, P. Davidson, L. Belloni, C. Levard, J. Rose, P. Launois, A. Thill, *Chem. Commun.* **2013**, *49*, 11284.
[29] E. Paineau, M.-E. M. Krapf, M.-S. Amara, N. V. Matskova, I. Dozov, S. Rouzière, A. Thill, P. Launois, P. Davidson, *Nat. Commun.* **2016**, *7*, 10271.
[30] C.-Y. Su, Q. Lyu, D.-Y. Kang, Z.-H. Yang, C. H. Lam, Y.-H. Chen, S.-C. Lo, C.-C. Hua, L.-C. Lin, *Phys. Rev. Lett.* **2019**, *123*, 238002.
[31] E. Paineau, S. Rouzière, G. Monet, C. C. Diogo, I. Morfin, P. Launois, *J. Colloid Interface Sci.* **2020**, *580*, 275.
[32] W. J. Lee, E. Paineau, D. B. Anthony, Y. Gao, H. S. Leese, S. Rouzière, P. Launois, M. S. P. Shaffer, *ACS Nano* **2020**, *14*, 5570.
[33] J. F. Moore, E. Paineau, P. Launois, M. S. P. Shaffer, *ACS Appl Mater Interfaces* **2021**, *13*, 17940.
[34] F. Bourdelle, L. Truche, I. Pignatelli, R. Mosser-Ruck, C. Lorgeoux, C. Roszypal, N. Michau, *Chem. Geol.* **2014**, *381*, 194.
[35] C. Ruckebusch, L. Blanchet, *Anal. Chim. Acta* **2013**, *765*, 28.
[36] J. Jaumot, A. de Juan, R. Tauler, *Chemom. Intell. Lab. Syst.* **2015**, *140*, 1.
[37] E. Paineau, G. Monet, V. Peyre, C. Goldmann, S. Rouzière, P. Launois, *Langmuir* **2019**, *35*, 12451.
[38] R. Vogels, J. T. Kloprogge, J. W. Geus, *J. Colloid Interface Sci.* **2005**, *285*, 86.
[39] N. Arancibia-Miranda, M. Escudey, M. Molina, M. Teresa Garcia-Gonzalez, *J. Non-Cryst. Solids* **2011**, *357*, 1750.
[40] J.-P. Jolivet, C. Chaneac, D. Chiche, S. Cassaignon, O. Durupthy, J. Hernandez, *Comptes Rendus Geosci.* **2011**, *343*, 113.
[41] M. A. Wilson, G. S. H. Lee, R. C. Taylor, *J. Non-Cryst. Solids* **2001**, *296*, 172.
[42] H. Yang, C. Wang, Z. Su, *Chem. Mater.* **2008**, *20*, 4484.
[43] J. Cambedouzou, M. Chorro, R. Almairac, L. Noé, E. Flahaut, S. Rols, M. Monthioux, P. Launois, *Phys. Rev. B* **2009**, *79*, 195423.
[44] M. S. Amara, S. Rouziere, E. Paineau, M. Bacia-Verloop, A. Thill, P. Launois, *J. Phys. Chem. C* **2014**, *118*, 9299.
[45] J. L. Bishop, E. B. Rampe, D. L. Bish, Z. Abidin, L. L. Baker, N. Matsue, T. Henmi, *Clays Clay Miner.* **2013**, *61*, 57.
[46] I. Vicente, P. Salagre, Y. Cesteros, F. Medina, J. E. Sueiras, *Appl. Clay Sci.* **2010**, *48*, 26.
[47] A. Thill, B. Guiose, M. Bacia-Verloop, V. Geertsen, L. Belloni, *J. Phys. Chem. C* **2012**, *116*, 26841.
[48] E. Paineau, M. S. Amara, G. Monet, V. Peyre, S. Rouzière, P. Launois, *J. Phys. Chem. C* **2017**, *121*, 21740.
[49] S. Wada, K. Wada, *Clays Clay Miner.* **1982**, *30*, 123.

[50] E. Paineau, P. Launois, *Crystals* **2020**, *10*, 1094.
[51] P. Ildefonse, R. Kirkpatrick, B. Montez, G. Calas, A. Flank, P. Lagarde, *Clays Clay Miner.* **1994**, *42*, 276.
[52] G. Monet, S. Rouzière, D. Vantelon, C. Coelho Diogo, D. Maurin, J.-L. Bantignies, P. Launois, E. Paineau, *J. Phys. Chem. C* **2021**, *125*, 12414.
[53] A. Voronov, A. Urakawa, W. van Beek, N. E. Tsakoumis, H. Emerich, M. Rønning, *Anal. Chim. Acta* **2014**, *840*, 20.
[54] W. H. Cassinelli, L. Martins, A. R. Passos, S. H. Pulcinelli, C. V. Santilli, A. Rochet, V. Briois, *Catal. Today* **2014**, *229*, 114.
[55] D. Vantelon, M. Davranche, R. Marsac, C. La Fontaine, H. Guénet, J. Jestin, G. Campaore, A. Beauvois, V. Briois, *Environ. Sci. Nano* **2019**, *6*, 2641.
[56] W. Windig, J. Guilment, *Anal. Chem.* **1991**, *63*, 1425.
[57] F. C. Sánchez, B. Van den Bogaert, S. C. Rutan, D. L. Massart, *Chemom. Intell. Lab. Syst.* **1996**, *34*, 139.
[58] G. S. Pokrovski, J. Roux, J.-L. Hazemann, D. Testemale, *Chem. Geol.* **2005**, *217*, 127.
[59] S. Rouzière, V. Balédent, E. Paineau, E. Elkaim, T. Bizien, L. Nataf, Y. Pan, P. Launois, *Inorg. Chem.* **2023**.
[60] G. Monet, E. Paineau, Z. Chai, M. S. Amara, A. Orecchini, M. Jiménez-Ruiz, A. Ruiz-Caridad, L. Fine, S. Rouzière, L.-M. Liu, G. Teobaldi, S. Rols, P. Launois, *Nanoscale Adv.* **2020**, *2*, 1869.
[61] M. Li, J. A. Brant, *J. Membr. Sci.* **2019**, *585*, 38.
[62] I. Pignatelli, F. Bourdelle, D. Bartier, R. Mosser-Ruck, L. Truche, E. Mugnaioli, N. Michau, *Chem. Geol.* **2014**, *387*, 1.
[63] L. Truche, E. F. Bazarkina, G. Berger, M.-C. Caumon, G. Bessaque, J. Dubessy, *Geochim. Cosmochim. Acta* **2016**, *177*, 238.
[64] F. Bourdelle, R. Mosser-Ruck, L. Truche, C. Lorgeoux, I. Pignatelli, N. Michau, *Chem. Geol.* **2017**, *466*, 600.
[65] O. Tache, S. Rouziere, P. Joly, M. Amara, B. Fleury, A. Thill, P. Launois, O. Spalla, B. Abecassis, *J. Appl. Crystallogr.* **2016**, *49*, 1624.
[66] D. Vantelon, N. Trcera, D. Roy, T. Moreno, D. Mailly, S. Guilet, E. Metchalkov, F. Delmotte, B. Lassalle, P. Lagarde, *J. Synchrotron Radiat.* **2016**, *23*, 635.
[67] B. Ravel, M. Newville, *J. Synchrotron Radiat.* **2005**, *12*, 537.
[68] V. Briois, C. La Fontaine, S. Belin, L. Barthe, T. Moreno, V. Pinty, A. Carcy, R. Girardot, E. Fonda, in *J. Phys. Conf. Ser.*, IOP Publishing, **2016**, p. 012149.
[69] C. Lesage, E. Devers, C. Legens, G. Fernandes, O. Roudenko, V. Briois, *Catal. Today* **2019**, *336*, 63.